UMass Chan Medical School

eScholarship@UMassChan

2021-10-01

Molecular structure and conformation of stereocilia tip-links elucidated by cryo-electron tomography [preprint]

Johannes Elferich
UMass Chan Medical School

Et al.

Let us know how access to this document benefits you.

Repository Citation

Creative Commons License

1   9.30.2021

2

3   Molecular structure and conformation of stereocilia tip-links elucidated by cryo-electron

4   tomography

5   Johannes Elferich[1,2,3], Sarah Clark[1], Jingpeng Ge[1], April Goehring[1,3], Aya Matsui[1,3] and Eric

6   Gouaux[1,3,4]

7   [1]Vollum Institute, Oregon Health & Science University, 3181 SW Sam Jackson Park Road,

8   Portland, OR 97239

9   [2]RNA Therapeutics Institute, UMass Chan Medical School, 368 Plantation St, Worcester, MA

10   01605

11   [3]Howard Hughes Medical Institute, Portland, OR 97239

12   [4]Lead contact

13   *Correspondence: gouauxe@ohsu.edu

14

15

16

17   **Abstract**

18   Mechanosensory transduction (MT), the conversion of mechanical stimuli into electrical

19   signals, underpins hearing and balance and is carried out within hair cells in the inner ear. Hair

20   cells harbor actin-filled stereocilia, arranged in rows of descending heights, where the tips of

21   stereocilia are connected to their taller neighbors by a filament composed of protocadherin 15

22   (PCDH15) and cadherin 23 (CDH23), deemed the 'tip-link'. Tension exerted on the tip-link

23   opens an ion channel at the tip of the shorter stereocilia, thus converting mechanical force into an

24   electrical signal. While biochemical and structural studies have provided insights into the

25   molecular composition and structure of isolated portions of the tip-link, the architecture, location

26   and conformational states of intact tip-links, on stereocilia, remains unknown. Here we report *in*

27   *situ* cryo-electron microscopy imaging of the tip-link in mouse stereocilia. We observe

28   individual PCDH15 molecules at the tip and shaft of stereocilia and determine their

29   stoichiometry, conformational heterogeneity, and their complexes with CDH23. The

30   PCDH15/CDH23 complexes occur in clusters, frequently with more than one copy of PCDH15

31   at the tip of stereocilia, suggesting that tip-links might consist of more than one copy of the

32   PCDH15/CDH23 heterotetramer and by extension, might include multiple MT complexes.

33

34

Introduction

Vertebrates sense sound, movement and balance using specialized sensory neurons, called hair cells (McPherson, 2018). In mammals, hair cells are found in the inner ear and are organized in several specialized organs. Examples include the cochlea, which senses sound, and the utricle, which contributes to balance sensation (Ekdale, 2016). Hair cells harbor sensory microvili at their apical surface, which are called stereocilia. Stereocilia are rigid, due to being filled with crosslinked actin filaments (Tilney et al., 1992), and assemble in a staircase pattern in rows of descending height (Pickles et al., 1984). Upon deflection of the stereocilia staircase, tension is exerted on a filament connecting the tip of stereocilia with their taller neighbor, called the tip-link (Pickles et al., 1984). This tension then causes the opening of a channel, called the mechanosensory transduction (MT) channel, at the base of the tip-link (Zheng and Holt, 2021). The molecular mechanism of MT channel function, the conversion from mechanical to electrical signal in the inner ear, remains poorly understood.

The molecular nature of components of the MT machinery have been recently elucidated. The tip-link consists of the two-noncanonical cadherins protocadherin 15 (PCDH15) and cadherin 23 (CDH23) (Zheng and Holt, 2021). PCDH15 is situated at the tip of the shorter stereocilia and its two N-terminal cadherin domains bind to the two N-terminal cadherin domains of CDH23 (Kazmierczak et al., 2007; Sotomayor et al., 2012). The MT channel is likely formed by the transmembrane-channel like (TMC) protein 1 or 2 and the transmembrane protein of the inner ear (TMIE) (Zheng and Holt, 2021). PCDH15 assembles in the membrane together with lipoma HMGIC Fusion Partner-Like 5 (LHFPL5,TMHS) (Ge et al., 2018, p. 5) and pull-down studies using protein fragments suggest that PCDH15 may also interact with TMC-1 (Maeda et al., 2014). PCDH15 is also theorized to interact with the cytoskeleton via whirlin (Michel et al.,

58   2020), while TMC may be coupled to the cytoskeleton via CIB2 and ankyrin repeats (Tang et al.,

59   2020). However, the molecular composition of the MT machinery and the 3D arrangements of

60   each component remain unknown.

61   The fundamental transduction activity of the MT machinery is the conversion of force

62   into an electrical signal (Hudspeth, 1989). Indeed, the mechanical displacement of the stereocilia

63   can be modeled using Hooke's Law, suggesting the presence of an elastic element, or a 'gating

64   spring', that couples displacement to the ion channel opening (Howard and Hudspeth, 1987). On

65   the one hand, elasticity measurements of PCDH15 suggest that the tip-link itself acts as the

66   gating-spring (Bartsch et al., 2019), while on the other hand the plasma membrane at the tip of

67   stereocilia, as well as elements that couple the tip-link to the cytoskeleton, are other candidates to

68   act as 'elastic elements' (Powers et al., 2012). Therefore, insights into the molecular structure

69   and dynamics of the tip-link are essential for understanding mechanosensory transduction.

70   The molecular unit of the tip-link is a heterotetramer of PCDH15 and CDH23, where

71   both cadherins form a parallel dimer (Dionne et al., 2018) and come together as a dimer-of-

72   dimers using an anti-parallel 'handshake' of EC-1 and 2 of both cadherins (Sotomayor et al.,

73   2012). The extracellular domains of both PCDH15 and CDH23 are a chain of cadherin domains

74   with 11 and 27 repeats, respectively. Canonical cadherin domains form a 'stiff' dimer in the

75   presence of calcium, due to stabilizing calcium binding sites in the linker regions between

76   cadherin domains (Marquis and Hudspeth, 1997). Both PCDH15 and CDH23 have non-

77   canonical linkers devoid of canonical calcium binding sites, thus likely promoting

78   conformational mobility (Araya-Secchi et al., 2016; Jaiganesh et al., 2018; Powers et al., 2017).

79   Notably, the linker between EC9 and EC10 of PCDH15 is flexible *in vitro,* allowing a bend of up

80   to 90° (Araya-Secchi et al., 2016; Ge et al., 2018). Bending and extension along this linker has

81   been suggested as underlying the elasticity of the gating spring (Araya-Secchi et al., 2016), yet

82   atomic force microscopy measurements and molecular dynamics simulations of PCDH15 also

83   have suggested that individual cadherin domains can unfold to give rise to tip-link extension

84   (De-la-Torre et al., 2018; Oroz et al., 2019). However, it is unclear which of these mechanisms

85   occur *in situ.*

86   The majority of our current knowledge about the assembly of the tip-link *in situ* is based

87   on fixed and stained scanning-electron microscopy (SEM) or freeze-fracture transmission

88   electron microscopy (TEM) of stereocilia (Kachar et al., 2000; Michel et al., 2005). These

89   images reveal a 120-170 nm long, helically coiled, filament with a diameter of 5 nm and a repeat

90   of 40 nm (Kachar et al., 2000). Furthermore, these links appear to bifurcate at the upper and

91   lower insertion sites into 2-3 individual strands, an observation that is difficult to reconcile in

92   light of high resolution structural data showing that PCDH15 and CDH23 are parallel dimers and

93   that both proteins also harbor membrane-proximal 'dimerization domains' (De-la-Torre et al.,

94   2018; Dionne et al., 2018; Ge et al., 2018). This may be because the imaging methods relied on

95   fixation and staining procedures, which are manipulations that can introduce artifacts or

96   distortions.

97   More recently, cryo-electron microscopy imaging has been used to image stereocilia in

98   their native state, avoiding these artifacts (Metlagel et al., 2019; Song et al., 2020). However, due

99   to rapid damage of the specimen by high-energy electrons, the contrast of this imaging modality

100   is low, making it challenging to visually identify relatively small features, such as the tip-link.

101   Therefore, labeling approaches are required to unambiguously identify components of the MT

102   machinery. In this study, we combine a stereocilia preparation technique for cryo-EM imaging

103   (Metlagel et al., 2019; Song et al., 2020) with a highly specific, immuno-affinity labeling

104   approach using anti-PCDH15 antibody-coupled gold nanoparticles (AuNP) (Azubel et al., 2019)

105   to elucidate the molecular structures and conformational states of tip-links, *in situ*, under native

106   conditions.

107   **Results**

108   **Cryo-CLEM imaging of immunolabeled stereocilia**

109   To develop tools to identify PCDH15 in cryo-electron tomograms, we raised polyclonal

110   antibodies (pAbs) against the entire extracellular region of mouse PCDH15. Immunostaining of

111   mouse cochlea using these anti PCDH15 pAbs produces punctate features at the tips of

112   stereocilia in hair cells derived from wild-type (WT) mice, features that are entirely absent from

113   the stereocilia of PCDH15 knock-out mice, thus demonstrating the specificity and utility of the

114   anti-PCDH15 pAbs (Figure 1A). We observed similar staining of stereocilia derived from mouse

115   utricles, both in the presence of calcium and after chelation of calcium using BAPTA, indicating

116   that the binding was independent of calcium and thus, also independent of the PCDH15-CDH23

117   'handshake' (Figure 1B). To facilitate the collection of a large dataset of tomograms focused on

118   the tip-region of stereocilia, we adopted a stereocilia preparation technique in which the sensory

119   epithelium is touched to holey carbon support film cryo-EM grids treated with poly-lysine, thus

120   enabling the deposition of stereocilia onto the grid (Metlagel et al., 2019). We subsequently

121   identified stereocilia by staining the sample with an actin dye and imaging with cryo-light

122   fluorescence microscopy (Figure 1C), allowing us to estimate the number of squares with a

123   favorable number of stereocilia and appropriate ice thickness. We then collected tomograms in

124   these squares, focusing on positions where the tips of stereocilia coincided with holes in the

125   holey carbon film (Figure 1C).

126   In initial experiments, we labeled stereocilia with the anti-PCDH15 pAbs using

127 secondary antibodies conjugated to 5 nm gold particles. In the resulting images, we clearly

128 visualized clusters of 5 nm gold particles in the images of some of the tips (Figure 1D). While

129 this validated our immuno-labeling approach, we were unable to determine the number of

130 PCDH15 molecules present due to the undefined stoichiometry of both the primary and

131 secondary reagent. Furthermore, the gold particles obstructed the direct observation of the

132 PCDH15 electron density.

133 **Preparation of a PCDH15 gold-labeling reagent with 1:1 stoichiometry**

134   To specifically label PCDH15 subunits with single gold particles, we developed a high

135 affinity, slow off-rate (k_{off} = 4.6 x 10^{-5} 1/s), anti-PCDH15 monoclonal antibody (mAb), deemed

136 39G7. By examining the binding of 39G7 to a series of PCDH15 truncation constructs, we

137 determined that the mAb binds to the EC3 cadherin domain, near the amino terminus (Figure

138 2A). Similar to the anti-PCDH15 pAbs, the 39G7 mAb stained PCDH15 on the surface of

139 vestibular stereocilia, either in the presence or absence of calcium (Figure 2B).

140   To create a reagent to label PCDH15 subunits with a single gold particle, we created a

141 39G7 Fab construct with a single free cysteine residue at the C terminus of the heavy chain, thus

142 enabling conjugation of the Fab to 3 nm AuNPs (Azubel et al., 2019, p. 2). Purification of the

143 39G7 Fab – AuNP complex via polyacrylamide electrophoresis and size exclusion

144 chromatography (SEC) yielded a homogeneous species in which the Fab was a labeled with a

145 single AuNP (Figure 2C+D), devoid of non AuNP-labeled Fabs. Using this reagent, we reasoned

146 that we could directly count PCDH15 subunits because only a single Fab will bind to each

147 PCDH15 subunit and each Fab is labeled by a single AuNP. We confirmed this prediction by

148 forming a complex between the 39G7 Fab – AuNP and recombinant PCDH15, isolating the

149   complex by SEC (Figure 2E) and imaging the complex by single particle cryo-EM (Figure 2F).

150   On micrographs and tomographic reconstructions (Movie S1), we clearly identified pairs of

151   AuNPs bound to the PCDH15 extracellular domain, consistent with a dimeric model of the

152   PCDH15 extracellular domain, the 39G7 Fab binding to EC3 and the ability of the Fab – AuNP

153   complex to allow us to identify and count PCDH15 subunits.

154   **39G7-AuNP labeling of stereocilia shows that PCDH15 is a dimer**

155   We prepared cryo-EM grids using utricles stained with 39G7 Fab-AuNP and collected

156   tomograms, primarily of stereocilia tips (Figure 3E). On approximately half of the tomograms

157   we identified 3 nm gold particles within ~38 nm of the stereocilia membrane, a distance that is

158   consistent with the binding of 39G7 to ECD3 of PCDH15. We also identified AuNP labels in

159   tomograms of the stereocilia shaft region, but only in about a third of the tomograms that

160   featured only stereocilia shaft regions. Close inspection of the electron density around the AuNPs

161   frequently revealed ~50 nm long filamentous density consistent with the extracellular domain of

162   PCDH15 (Figure 3A-B, Movie S2-3). In tomograms with relatively thin ice (<200 nm) and an

163   appropriate orientation of the filament to the tilt-axis, dimeric features of the PCDH15 domain

164   are evident that, together with the presence of the AuNP pairs with a distance of 20 nm,

165   demonstrates that PCDH15 forms a dimer *in situ.* In some cases, we observed individual gold

166   particles instead of a pair of AuNPs (Figure 3C-D, Movie S4-5) yet also dimeric features

167   associated with PCDH15 chain, thus indicating that the visualization of individual AuNPs was

168   likely due to incomplete labeling of PCDH15 and not the presence of PCDH15 monomers. We

169   quantified the occurrence of AuNP dimers and monomers (Figure 3F) and found a ratio of 3:1.

170   Under the assumption that bindings of the 39G7 Fab to either protomer are independent events,

171   we can use this ratio to estimate the fraction of PCDH15 protomers labeled with 39G7-AuNP

172   (0.86) and the fraction of PCDH15 dimers that are completely unlabeled (0.02). While this may

173   be an underestimation of the number of unlabeled PCDH15 molecules, either due to

174   cooperativity of 39G7 binding or due to air-water interface effects, it nevertheless demonstrates

175   that the 39G7 Fab-AuNP robustly labels PCDH15 *in situ* and therefore allows precise

176   quantification of the number of PCDH15 molecules at the tips of stereocilia.

Stereocilia tips harbor multiple copies of PCDH15

178   We carefully quantified the number of PCDH15 molecules in all imaged stereocilia tips

179   (n=396) (Figure 4F). Slightly more than half of the stereocilia tips (58%) did not contain a

180   PCDH15 label. While this could be due to an underestimate of the labeling efficiency or due to

181   preferential selection of stereocilia in the tallest row, we believe the most likely explanation is

182   damage to stereocilia tips during the blotting of stereocilia on the cryo-EM grids. In some cases

183   (5.8%), we found PCDH15 molecules in the shaft region just 'below' the stereocilia tips (Figure

184   4A, Movie S6). It is possible that these molecules were initially located on the tip, but diffused

185   away in the time between applying tissue to the grid and plunge-freezing. In 13% of tips we

186   found a single molecule of PCDH15 at the tip (Figure 4B+C, Movie S7-8), similar to commonly

187   depicted models of the MT complex. However, in almost twice the number of stereocilia tips

188   (23%) we found multiple copies of PCDH15 at the tip, either clustered at the tip (Figure 4D,

189   Movie S9) or spread across its surface (Figure 4E, Movie S10). Because we cannot determine

190   that maturity of the hair cells from which the stereocilia are derived, multiple PCDH15

191   molecules at the tips may be due to stereocilia derived from immature hair cells. Indeed, many

192   molecular models of the MT machinery posit the presence of one copy of the PCDH15 dimer

193   bound to a single MT-channel. Our data, however, suggests that many tips might harbor multiple

194   copies of the MT machinery, which in turn might underly variation in the ion channel

195   conductance at individual tips (Beurg et al., 2018).

196   **Tomographic reconstructions of PCDH15-CDH23 heterotetramers**

197   In a few tomograms, we found electron-density extending beyond the tip of PCDH15,

198   consistent with a 120 nm long filament inserted into two distinct membranes (Figure 5). While

199   we cannot determine the molecular identity of this density unambiguously, the dimensions of this

200   molecule suggest that the density corresponds to CDH23. In one example, we found a stereocilia

201   tip with 5 copies of a PCDH15 dimer, 3 of which were connected to a putative CDH23 density,

202   which in turn was inserted into a small spherical liposome (Figure 5A, Movie S11). Our

203   interpretation of this structure is that this was a tip-link assembly, disrupted during sample

204   preparation, where a portion of the membrane surrounding CDH23 was 'torn off' of the

205   neighboring stereocilia, yielding CDH23 bound to a liposome. In another case, a cluster of five

206   PCDH15 molecules close to a stereocilium tip is connected to four CDH23 densities inserted into

207   a lipid membrane fragment (Figure 5B, Movie S12).

208   We also observed structures in which it appears as though PCDH15, together with a fraction of

209   surrounding membrane, were extracted from the shorter stereocilium (Figure 5C+D, Movie S13-

210   14). In both cases we found 3-5 copies of PCDH15 and CDH23. The fact that we observed most

211   PCDH15/CDH23 complexes in structures that appear to be the result of partial damage of the

212   tip-link, is consistent with the earlier interpretation of the missing PCDH15 label is due to

213   damaged tip-links. It is also possible that clusters of PCDH15/CDH23 complexes are more stable

214   than isolated PCDH15/CDH23 complexes, and thus more frequently observed.

215

216

217 **An intact tip-link surrounded by non CDH23-bound PCDH15 molecules**

218   In one tomogram, we imaged the tip of a stereocilium situated next to a longer

219 stereocilium (Figure 6A, Movie S15). While we observed 17 AuNPs at the tip of the shorter

220 stereocilium, we only unambiguously identified the density for four PCDH15 molecules. On one

221 of these PCDH15 molecules we observed a 120 nm long filament, connecting PCDH15 to the

222 longer stereocilium (Figure 6B). We hypothesize that this is most likely an intact tip-link. Upon

223 closer inspection (Figure 6C), we can clearly identify dimeric features on this PCDH15

224 molecule. Other adjacent PCDH15 molecules are also clearly dimeric entities (Figure 6D), yet

225 are not bound to CDH23. Further down the two stereocilia we identified another copy of

226 PCDH15, apparently connected via CDH23 to the other stereocilium (Figure 6E). In this case

227 PCDH15 appears to be bent, by about 90°, at juncture of the EC9-EC10 cadherin domains, a

228 'joint' between cadherin domains that has previously been identified as flexible in cryo-EM and

229 crystallography structures of PCDH15 extracellular domain constructs (Araya-Secchi et al.,

230 2016; Ge et al., 2018). We speculate that this link may be in the process of being trafficked to the

231 tip and that the EC9-EC10 bend helps to accommodate the long filament within the relatively

232 narrow space between stereocilia.

233 **Lateral links consisting of PCDH15/CDH23**

234   While in the majority of tomograms we identified 10 or fewer copies of PCDH15, several

235 tomograms exhibit numbers of labels consistent with hundreds of copies of PCDH15. In the most

236 striking example (Figure 7A, Movie S16), we observed these labels between stereocilia that

237 appear thinner and less densely packed with actin than other stereocilia. In this tomogram we

238 counted 309 AuNPs and modeled 56 PCDH15 molecules in cases where we observed the

239 corresponding electron density. Many of the PCDH15 molecules are involved in links to

240   neighboring stereocilia, via a 120 nm filament, which again is likely CDH23. We observed

241   density for 20 putative CDH23 molecules, molecules which likely participate in the 'lateral

242   links' which form early in development of stereocilia bundles and are composed of PCDH15 and

243   CDH23 (Michel et al., 2005). Inspection of the densities shows that multiple copies of CDH23

244   cluster together, primarily via the N-terminal half of CDH23, so as to obscure identification of

245   individual stands (Figure 7B+C). We speculate that these clusters might have given rise to the

246   appearance of single tip-links with multiple upper and lower insertion points in stained EM

247   images. Furthermore, we find examples of CDH23 that appear bent half-way between the N- and

248   C-termini, indicating that CDH23 might also have a flexible cadherin domain 'joint', similar to

249   the EC9-EC10 interface of PCDH15 (Figure 7D). A potential candidate for this joint is the non-

250   canonical linker between EC12 and EC13 of CDH23 (Jaiganesh et al., 2018).

251   **Discussion**

252   The combination of cryo-EM and AuNP labeling provides a molecular resolution view of

253   the structure, stoichiometry, and organization of tip-links in their native environment. This work

254   is the first look at native tip-links *in situ*, as previous studies relied on microscopy of fixed and

255   stained specimens, which have an inherently lower resolution and are prone to artifacts

256   (Indzhykulian et al., 2013; Kachar et al., 2000; Michel et al., 2005).

257   We observe clusters of PCDH15-CDH23 complexes on the stereocilia tip and shaft, as

258   well as multiple copies of PCDH15 at stereocilia tips, ranging from two to more than five.

259   Because the majority of the PCDH15 molecules we observed were not bound to CDH23 to form

260   an intact tip-link, the mechanistic underpinnings of multiple PCDH15 molecules, if any, are

261   unclear. One possibility is that each PCDH15 molecule was coupled to a functional MT channel

262   and the tip-link was ruptured during cryo-EM grid preparation. This would imply that there are

263   multiple MT complexes per stereocilia tip, as suggested previously (Beurg et al., 2018).

264   Confocal microscopy images of stereocilia expressing mCherry-tagged TMC1 indicate that there

265   are an average of 7.1 TMC1 channels per stereocilia tip derived from the inner hair cells of P4

266   aged mice. The number of TMC1 per stereocilia tip varies from four to twenty depending on the

267   cochlear localization, mirroring the high degree of variability we observed for PCDH15.

268   It is also possible that a large number of PCDH15 molecules may be necessary for

269   rebinding to CDH23 in the event of tip-link breakage. Atomic force microscopy experiments

270   indicate that the lifetime of the PCDH15-CDH23 bond is only ~8 seconds at resting tension,

271   suggesting that the tip-link is a highly dynamic connection (Mulhall et al., 2021). A pool of

272   nearby PCDH15 molecules may enable fast recovery after tip-links are broken. It has also been

273   suggested that intermediate PCDH15-PCDH15 tips form first during tip-link regeneration,

274   followed by mature PCDH15-CDH23 tip-links, necessitating the presence of multiple PCDH15

275   molecules (Indzhykulian et al., 2013).

276   Our tomograms also revealed distinct structural features of PCDH15 and CDH23. Most

277   intact tip-links were approximately straight, ~120 nm length PCDH15-CDH23 heterotetramers

278   consisting of a PCDH15 dimer joined to a CDH23 dimer. However, in several tip-links, we

279   observed a ~90º bend in PCDH15 or CDH23. PCDH15 is bent at approximately the EC9-EC10

280   interface, which has been identified as flexible in cryo-EM and crystal structures of recombinant

281   PCDH15, while CDH23 appears to be bent near EC13. Crystal structures of CDH23 identified

282   non-canonical linker regions and altered Ca^{2+} binding sites within this region, motifs that could

283   confer increased flexibility (Jaiganesh et al., 2018). Furthermore, we often observe a 'splitting'

284   of the CDH23 dimer at various points, most frequently at the C-terminal end. This type of

285   structural heterogeneity is not observed for PCDH15. Crystallography studies of CDH23 have

286 noted a curious lack of multimerization interfaces between CDH23 protomers, consistent with

287 our observations, yet a rationale for minimal interchain CDH23 interactions remains to be

288 determined (Jaiganesh et al., 2018), other than to reduce likelihood of CDH23 aggregation.

289   In selected stereocilia, we note that the high densities of lateral PCDH15-CDH23 links

290 are consistent with our capture of an immature hair bundle. While the utricles employed in our

291 study were isolated from P6-9 mice, lateral links are still present until approximately P9

292 (Goodyear et al., 2005). These extensive lateral links stabilize the stereocilia during the early

293 stages of development by acting as a cohesive tethers, gradually being pruned until only the tip-

294 link remains in a mature hair bundle (Boëda et al., 2002; Michel et al., 2005).

295   Our work highlights the power of gold immunolabeling and cryo-EM to study rare

296 protein complexes. The MT complex is notorious for its low abundance, conspiring to make

297 studies of the mechanism of MT channel gating by tip-link tension challenging. The images

298 presented here reveal structural features of the MT machinery and demonstrate that the employed

299 techniques can be used to visualize single molecules in their native environment. It will be

300 exciting to use this technique to explore additional components of the MT complex, including

301 TMC1 and TMIE, in order to define their locations, stoichiometries and structures within the

302 architecture of the MT machinery.

303 **Methods**

304 **PCDH15 EC1-EL expression and purification**

305   A gene encoding the amino acid sequence of the mouse PCDH15 extracellular region

306 (Uniprot entry Q99PJ1), from the first cadherin domain (EC1) to the membrane-proximal 'EL'

307 domain (PCDH15 EC1-EL), was synthesized and cloned into a pBacMam vector (Goehring et

308 al., 2014), and included a C-terminal yellow fluorescent protein (YFP) fluorophore followed by a

309   polyhistidine tag. This construct was used to generate baculovirus, which was then employed to

310   infect HEK293 cells as previously described (Goehring et al., 2014). Approximately 96 hours

311   after viral transduction, the cell medium was harvested and the secreted PCDH15 EC1-EL

312   protein was isolated by metal ion affinity chromatography, and further purified by size exclusion

313   chromatography (SEC) in TBS Buffer (20 mM Tris pH8, 150 mM NaCl). The final material was

314   concentrated to ~ 2mg/ml, aliquoted and stored at -80 °C.

315   **Antibody generation**

316   Rabbit polyclonal and monoclonal antibodies were generated using standard techniques

317   by Genscript using the soluble PCDH15 EC1-EL extracellular region as the antigen. Polyclonal

318   serum was used to isolate antibodies using affinity-purification with the PCDH15 EC1-EL

319   extracellular domain. Hybridoma supernatants were screened against the PCDH15 EC1-EL

320   antigen in the presence and absence of 1 mM calcium to identify clones that recognize the

321   calcium-bound and apo forms of the protein. Supernatants that tested positive by ELISA were

322   further screened by fluorescence detection chromatography (FSEC) and Western blot and the

323   clone 39G7 was sequenced and monoclonal antibody was produced recombinantly.

324   **Immunofluorescence**

325   Cochlea and utricles were dissected from mice at ages P6-9 in DMEM/F12 media

326   (Gibco). The tissue was incubated for 30 minutes in 10 ug/ml of indicated antibody in

327   DMEM/F12 media, followed by washing, 3 times for 10 minutes each, in the same media.

328   Where indicated, 5 mM BAPTA was included in staining and washing media to chelate calcium.

329   The tissue was next fixed with in a buffer composed of 4% paraformaldehyde in phosphate-

330   buffered saline (PBS) for 10 minutes. After 3 washes in PBS, the tissue was permeabilized and

331   blocked using PBS with 0.1% Triton X-100, 5% bovine serum albumin (BSA), and 10%

332   standard goat serum. Subsequently, the tissue was stained with goat-anti-rabbit antibodies fused

333   to Alexa-594 and phalloidin fused to Alexa-405. After 3 washes with PBS, the tissue was

334   mounted with Vectashield mounting media and imaged using a Zeiss LSM 980 confocal

335   microscope using a 63x/1.49 NA objective.

336   **AuNP generation**

337   A solution of 84 mM 3-mercaptobenzoic acid (3-MBA) in methanol was mixed with a 28

338   mM solution of $HAuCl_4$ in methanol at 7:1 molar ratio, followed by 2.5 volumes of water. The

339   pH was adjusted by adding concentrated aqueous NaOH to a final concentration of 100 mM.

340   This solution was mixed by end-over-end rotation for at least 16 hours. Afterwards, the solution

341   was diluted with 27% methanol to achieve a final concentration of 2.5 mM 3-MBA. $NaBH_4$ was

342   added to a final concentration of 2 mM using a fresh 150 mM stock solution prepared in 10 mM

343   NaOH. After mixing for 4.5 hours, the gold particles were precipitated by adjusting the NaCl

344   concentration to 100 mM and by adding methanol to a final concentration of 70%. Gold AuNPs

345   were pelleted by centrifugation at 5,000 rpm for 20 minutes and washed with 70% methanol. The

346   pellet was dried overnight in a desiccator and re-suspended in water.

347   An expression construct for a Fab' fragment of 39G7 was designed using a dual-promoter

348   Sf9-expression plasmid (Vectorbuilder). For the 39G7 light chain, we replaced the native signal

349   peptide with the GP64 signal peptide and inserted the coding sequence downstream of the pH

350   promoter. For the 39G7 heavy chain, we replaced the native signal peptide with the GP64 signal

351   peptide and truncated the coding sequence after G256, thereby removing the Fc fragment but

352   retaining C243 and C248 at the C-terminus. The coding sequenced was then inserted after the

353   P10 promoter and fused with a histidine tag at the C-terminus. The 39G7 Fab' was expressed in

354   Sf9 cells for 96 hours at 27 °C. The media was adjusted to pH 8, cleared by centrifugation and

355   then concentrated to about 100 ml using a tangential-flow concentrator. The concentrated media

356   was pumped over a 5 ml metal ion affinity column, equilibrated with PBS. The column was

357   washed extensively with PBS supplemented with 30 mM imidazole and Fab' was eluted with

358   PBS supplemented with 500 mM imidazole. The yield was 2 mg of Fab' per liter of culture. The

359   pooled fractions were concentrated to 5 mg/ml and aliquots were plunge-frozen in liquid

360   nitrogen and stored at -80 °C.

361   To conjugate the Fab to the AuNPs, an aliquot of 39G7 Fab' was thawed and incubated

362   with 2 mM tris (2-carboxyethyl) phosphine hydrochloride (TCEP) for 1 hour at 37 °C. After

363   clarification by ultracentrifugation, the 39G7 Fab was applied to a SEC column equilibrated with

364   TBE buffer (100 mM Tris, 100mM boric acid, 2mM EDTA). The peak fractions were

365   concentrated immediately to 2 mg/ml and a test conjugation was set up at different molar ratios

366   of Fab' and AuNP (4:1,2:1,1:1,1:2,1:4). After a 30-minute incubation at 37 °C, the reactions were

367   analyzed on a 12.5% PAGE gel made with TBE and 10% glycerol. The condition with the

368   highest yield of the 1:1 AuNP/Fab complex was chosen for large scale conjugation. To coat the

369   AuNPs with PEG, the conjugate was immediately separated on a PAGE gel following and 1:1

370   39G7:AuNP recovered in TB buffer. After concentration, 1 mM of mPEG550-SH was added and

371   incubated for 60 minutes at 37 °C. The conjugate was then purified by SEC using a Superose 6

372   column equilibrated with PBS. Fractions corresponding to 39G7-AuNP conjugate were pooled,

373   concentrated to 1 µM (assuming an extinction coefficient of 3×10^6 (M^{-1} cm^{-1}) at 500 nm) and

374   stored at 4 °C.

Grid preparation

Utricles were dissected from P8-P11 mice in DMEM/F12 buffer. Otoconia were removed using an eyelash. Utricles were incubated for 30 minutes in DME M/F12 containing 100 nM 39G7-AuNP and 500 nM SirActin and then washed three times for 5 minutes in DMEM/F12. Utricles were then placed stereocilia-side down on C-Flat 200 mesh copper grids with a 2/1 spacing carbon film that were pretreated with 0.1 mg/ml poly-D-lysine and suspended in 20 ul drops of DMEM/F12. After 2-3 seconds, the utricle was removed and placed on another region of the grid for up to three times. The grid was removed 'edge-first' from the drop and excess liquid was removed by touching the edge to a piece of Whatman No. 40 filter paper. A 2.5 ul drop of DMEM/F12 containing 0.05% fluorinated octyl-maltoside and 10 nm highly uniform gold fiducials at an OD_{500} of roughly 5.0 were added to the grid. The grid was then placed on a manual blotting apparatus and excess solution was removed by placing a 595 filter paper (TED-Pella) for 6-10 seconds to the side of the grid without sample. Afterwards, the grid was rapidly plunged into a mixture of ethane and propane cooled to liquid nitrogen temperature. Grids were imaged in a CMS196 cryostage (Linkam) on a LSM880 confocal microscope (Zeiss) using the AiryScan detector. Grids that did not exhibit SirActin fluorescence in multiple squares, or had excessive damage to the carbon support, were discarded.**Tilt-series acquisition**

Tilt-series of the recombinant PCDH15 ECD1-EL extracellular region labeled with the 9G7-AuNP was acquired using a Thermo Fisher Arctica microscope operated at 200 keV, without an energy filter, on a Gatan K3 detector. Tilt-series of stereocilia were obtained on a Thermo Fisher Krios microscope operated at 300 keV with an energy filter on a Gatan K3 detector. A subset of tomograms were obtained from a Krios microscope also equipped with a spherical aberration corrector.

398   In all cases, tilt-series were obtained from -60 to 60 degrees using a 3-degree interval

399 using SerialEM. Data was either acquired by sweeping from -30 to 60 degrees and then from -30

400 to -60 degrees or by using a grouped dose symmetric scheme. In all cases the total electron dose

401 was 80-120 e-/A^2. Defocus was varied between -2.5 and -4.0 um.

Tomography processing

403   Tomograms were reconstructed using the IMOD program (Mastronarde and Held, 2017),

404 employing the 10 nm gold fiducials for alignment. In some cases, the 3 nm AuNP label was also

405 included as a fiducial. The tilt series was binned by 4 to a final pixel size of 6.6 A, CTF

406 corrected, the 10 nm gold particles were subtracted, and the tilt-series was dose-weighted.

407 Tomograms were reconstructed using a SIRT-like filter with 8 iterations. In cases where a

408 substantial amount of sample deformation was observed, tomograms were reconstructed using

409 the tomoalign program (Fernandez et al., 2019), using polynomials and the 'thick' preset. If

410 indicated, tomograms were denoised using the denoise3d model of Topaz (Bepler et al., 2020).

Tomogram annotation

412   Membranes were annotated manually in XY slices using the 3dmod program (Kremer et

413 al., 1996). Actin filaments were manually annotated in 26.4 nm thick slices perpendicular to the

414 stereocilium length. AuNP nanoparticles were either manually annotated or annotated using the

415 findbeads3d program of the IMOD suite. PCDH15 was positioned by identifying the membrane

416 insertion point and the PCDH15 tip in the 'Slicer' windows of the 3dmod program. The density

417 of the PCDH15 model was then aligned along these two points and, in some cases, was rotated

418 until the projection matched the density visible in the slicer window. Actin filaments were

419 manually annotated in slices perpendicular to the stereocilia axis using 3dmod. A low-pass

420 filtered electron-density of actin was placed along the annotated filaments using the

421   clonevolumes program. The final render of each model was performed using USCF ChimeraX

422   (Pettersen et al., 2021).

423   **Data availability**

424   Tomograms depicted in the figures have been deposited in the EMDB under accession

425   codes EMD-25046, EMD-25047, EMD-25048, EMD-25049, EMD-25050, EMD-25051, EMD-

426   25052, EMD-25053, EMD-25054, EMD-25055, EMD-25056, EMD-25057, EMD-25058, EMD-

427   25059, EMD-25060, and EMD-25061 (in order of appearance). The corresponding tilt-series

428   have been deposited in EMPIAR under accession code EMPIAR-10820. Other raw data is

429   available from the authors upon request.

430   **Acknowledgments**

439   **References**

440   Araya-Secchi R, Neel BL, Sotomayor M. 2016. An elastic element in the protocadherin-15 tip
441   link of the inner ear. *Nat Commun* **7**:13458. doi:10.1038/ncomms13458
442   Azubel M, Carter SD, Weiszmann J, Zhang J, Jensen GJ, Li Y, Kornberg RD. 2019. FGF21
443   trafficking in intact human cells revealed by cryo-electron tomography with gold
444   nanoparticles. *eLife* **8**:e43146. doi:10.7554/eLife.43146
445   Bartsch TF, Hengel FE, Oswald A, Dionne G, Chipendo IV, Mangat SS, El Shatanofy M,
446   Shapiro L, Müller U, Hudspeth AJ. 2019. Elasticity of individual protocadherin 15

447   molecules implicates tip links as the gating springs for hearing. *Proc Natl Acad Sci U S A*
448   **116**:11048–11056. doi:10.1073/pnas.1902163116
449   Bepler T, Kelley K, Noble AJ, Berger B. 2020. Topaz-Denoise: general deep denoising models
450   for cryoEM and cryoET. *Nat Commun* **11**:5208. doi:10.1038/s41467-020-18952-1
451   Beurg M, Cui R, Goldring AC, Ebrahim S, Fettiplace R, Kachar B. 2018. Variable number of
452   TMC1-dependent mechanotransducer channels underlie tonotopic conductance gradients
453   in the cochlea. *Nat Commun* **9**:2185. doi:10.1038/s41467-018-04589-8
454   Boëda B, El-Amraoui A, Bahloul A, Goodyear R, Daviet L, Blanchard S, Perfettini I, Fath KR,
455   Shorte S, Reiners J, Houdusse A, Legrain P, Wolfrum U, Richardson G, Petit C. 2002.
456   Myosin VIIa, harmonin and cadherin 23, three Usher I gene products that cooperate to
457   shape the sensory hair cell bundle. *EMBO J* **21**:6689–6699. doi:10.1093/emboj/cdf689
458   De-la-Torre P, Choudhary D, Araya-Secchi R, Narui Y, Sotomayor M. 2018. A Mechanically
459   Weak Extracellular Membrane-Adjacent Domain Induces Dimerization of Protocadherin-
460   15. *Biophys J* **115**:2368–2385. doi:10.1016/j.bpj.2018.11.010
461   Dionne G, Qiu X, Rapp M, Liang X, Zhao B, Peng G, Katsamba PS, Ahlsen G, Rubinstein R,
462   Potter CS, Carragher B, Honig B, Müller U, Shapiro L. 2018. Mechanotransduction by
463   PCDH15 Relies on a Novel cis-Dimeric Architecture. *Neuron* **99**:480-492.e5.
464   doi:10.1016/j.neuron.2018.07.006
465   Ekdale EG. 2016. Form and function of the mammalian inner ear. *J Anat* **228**:324–337.
466   doi:10.1111/joa.12308
467   Fernandez J-J, Li S, Agard DA. 2019. Consideration of sample motion in cryo-tomography
468   based on alignment residual interpolation. *J Struct Biol* **205**:1–6.
469   doi:10.1016/j.jsb.2019.01.005
470   Ge J, Elferich J, Goehring A, Zhao H, Schuck P, Gouaux E. 2018. Structure of mouse
471   protocadherin 15 of the stereocilia tip link in complex with LHFPL5. *eLife* **7**:e38770.
472   doi:10.7554/eLife.38770
473   Goehring A, Lee C-H, Wang KH, Michel JC, Claxton DP, Baconguis I, Althoff T, Fischer S,
474   Garcia KC, Gouaux E. 2014. Screening and large-scale expression of membrane proteins
475   in mammalian cells for structural studies. *Nat Protoc* **9**:2574–2585.
476   doi:10.1038/nprot.2014.173
477   Goodyear RJ, Marcotti W, Kros CJ, Richardson GP. 2005. Development and properties of
478   stereociliary link types in hair cells of the mouse cochlea. *J Comp Neurol* **485**:75–85.
479   doi:10.1002/cne.20513
480   Howard J, Hudspeth AJ. 1987. Mechanical relaxation of the hair bundle mediates adaptation in
481   mechanoelectrical transduction by the bullfrog's saccular hair cell. *Proc Natl Acad Sci*
482   **84**:3064–3068. doi:10.1073/pnas.84.9.3064
483   Hudspeth AJ. 1989. How the ear's works work. *Nature* **341**:397–404. doi:10.1038/341397a0
484   Indzhykulian AA, Stepanyan R, Nelina A, Spinelli KJ, Ahmed ZM, Belyantseva IA, Friedman
485   TB, Barr-Gillespie PG, Frolenkov GI. 2013. Molecular remodeling of tip links underlies
486   mechanosensory regeneration in auditory hair cells. *PLoS Biol* **11**:e1001583.
487   doi:10.1371/journal.pbio.1001583
488   Jaiganesh A, De-la-Torre P, Patel AA, Termine DJ, Velez-Cortes F, Chen C, Sotomayor M.
489   2018. Zooming in on Cadherin-23: Structural Diversity and Potential Mechanisms of
490   Inherited Deafness. *Struct Lond Engl 1993* **26**:1210-1225.e4.
491   doi:10.1016/j.str.2018.06.003

492 Kachar B, Parakkal M, Kurc M, Zhao Y, Gillespie PG. 2000. High-resolution structure of hair-
493 cell tip links. *Proc Natl Acad Sci U S A* **97**:13336–13341. doi:10.1073/pnas.97.24.13336
494 Kazmierczak P, Sakaguchi H, Tokita J, Wilson-Kubalek EM, Milligan RA, Müller U, Kachar B.
495 2007. Cadherin 23 and protocadherin 15 interact to form tip-link filaments in sensory hair
496 cells. *Nature* **449**:87–91. doi:10.1038/nature06091
497 Kremer JR, Mastronarde DN, McIntosh JR. 1996. Computer visualization of three-dimensional
498 image data using IMOD. *J Struct Biol* **116**:71–76. doi:10.1006/jsbi.1996.0013
499 Maeda R, Kindt KS, Mo W, Morgan CP, Erickson T, Zhao H, Clemens-Grisham R, Barr-
500 Gillespie PG, Nicolson T. 2014. Tip-link protein protocadherin 15 interacts with
501 transmembrane channel-like proteins TMC1 and TMC2. *Proc Natl Acad Sci U S A*
502 **111**:12907–12912. doi:10.1073/pnas.1402152111
503 Marquis RE, Hudspeth AJ. 1997. Effects of extracellular Ca2+ concentration on hair-bundle
504 stiffness and gating-spring integrity in hair cells. *Proc Natl Acad Sci* **94**:11923–11928.
505 doi:10.1073/pnas.94.22.11923
506 Mastronarde DN, Held SR. 2017. Automated tilt series alignment and tomographic
507 reconstruction in IMOD. *J Struct Biol*, Electron Tomography **197**:102–113.
508 doi:10.1016/j.jsb.2016.07.011
509 McPherson DR. 2018. Sensory Hair Cells: An Introduction to Structure and Physiology. *Integr*
510 *Comp Biol* **58**:282–300. doi:10.1093/icb/icy064
511 Metlagel Z, Krey JF, Song J, Swift MF, Tivol WJ, Dumont RA, Thai J, Chang A, Seifikar H,
512 Volkmann N, Hanein D, Barr-Gillespie PG, Auer M. 2019. Electron cryo-tomography of
513 vestibular hair-cell stereocilia. *J Struct Biol* **206**:149–155. doi:10.1016/j.jsb.2019.02.006
514 Michel V, Goodyear RJ, Weil D, Marcotti W, Perfettini I, Wolfrum U, Kros CJ, Richardson GP,
515 Petit C. 2005. Cadherin 23 is a component of the transient lateral links in the developing
516 hair bundles of cochlear sensory cells. *Dev Biol* **280**:281–294.
517 doi:10.1016/j.ydbio.2005.01.014
518 Michel V, Pepermans E, Boutet de Monvel J, England P, Nouaille S, Aghaie A, Delhommel F,
519 Wolff N, Perfettini I, Hardelin J-P, Petit C, Bahloul A. 2020. Interaction of
520 protocadherin-15 with the scaffold protein whirlin supports its anchoring of hair-bundle
521 lateral links in cochlear hair cells. *Sci Rep* **10**:16430. doi:10.1038/s41598-020-73158-1
522 Mulhall EM, Ward A, Yang D, Koussa MA, Corey DP, Wong WP. 2021. Single-molecule force
523 spectroscopy reveals the dynamic strength of the hair-cell tip-link connection. *Nat*
524 *Commun* **12**:849. doi:10.1038/s41467-021-21033-6
525 Oroz J, Galera-Prat A, Hervás R, Valbuena A, Fernández-Bravo D, Carrión-Vázquez M. 2019.
526 Nanomechanics of tip-link cadherins. *Sci Rep* **9**:13306. doi:10.1038/s41598-019-49518-x
527 Pettersen EF, Goddard TD, Huang CC, Meng EC, Couch GS, Croll TI, Morris JH, Ferrin TE.
528 2021. UCSF ChimeraX: Structure visualization for researchers, educators, and
529 developers. *Protein Sci Publ Protein Soc* **30**:70–82. doi:10.1002/pro.3943
530 Pickles JO, Comis SD, Osborne MP. 1984. Cross-links between stereocilia in the guinea pig
531 organ of Corti, and their possible relation to sensory transduction. *Hear Res* **15**:103–112.
532 doi:10.1016/0378-5955(84)90041-8
533 Powers RE, Gaudet R, Sotomayor M. 2017. A Partial Calcium-Free Linker Confers Flexibility to
534 Inner-Ear Protocadherin-15. *Struct Lond Engl 1993* **25**:482–495.
535 doi:10.1016/j.str.2017.01.014

536   Powers RJ, Roy S, Atilgan E, Brownell WE, Sun SX, Gillespie PG, Spector AA. 2012.
537   Stereocilia Membrane Deformation: Implications for the Gating Spring and
538   Mechanotransduction Channel. *Biophys J* **102**:201–210. doi:10.1016/j.bpj.2011.12.022
539   Song J, Patterson R, Metlagel Z, Krey JF, Hao S, Wang L, Ng B, Sazzed S, Kovacs J, Wriggers
540   W, He J, Barr-Gillespie PG, Auer M. 2020. A cryo-tomography-based volumetric model
541   of the actin core of mouse vestibular hair cell stereocilia lacking plastin 1. *J Struct Biol*
542   **210**:107461. doi:10.1016/j.jsb.2020.107461
543   Sotomayor M, Weihofen WA, Gaudet R, Corey DP. 2012. Structure of a force-conveying
544   cadherin bond essential for inner-ear mechanotransduction. *Nature* **492**:128–132.
545   doi:10.1038/nature11590
546   Tang Y-Q, Lee SA, Rahman M, Vanapalli SA, Lu H, Schafer WR. 2020. Ankyrin Is An
547   Intracellular Tether for TMC Mechanotransduction Channels. *Neuron* **107**:112-125.e10.
548   doi:10.1016/j.neuron.2020.03.026
549   Tilney LG, Tilney MS, DeRosier DJ. 1992. Actin filaments, stereocilia, and hair cells: how cells
550   count and measure. *Annu Rev Cell Biol* **8**:257–274.
551   doi:10.1146/annurev.cb.08.110192.001353
552   Zheng W, Holt JR. 2021. The Mechanosensory Transduction Machinery in Inner Ear Hair Cells.
553   *Annu Rev Biophys* **50**:31–51. doi:10.1146/annurev-biophys-062420-081842
554
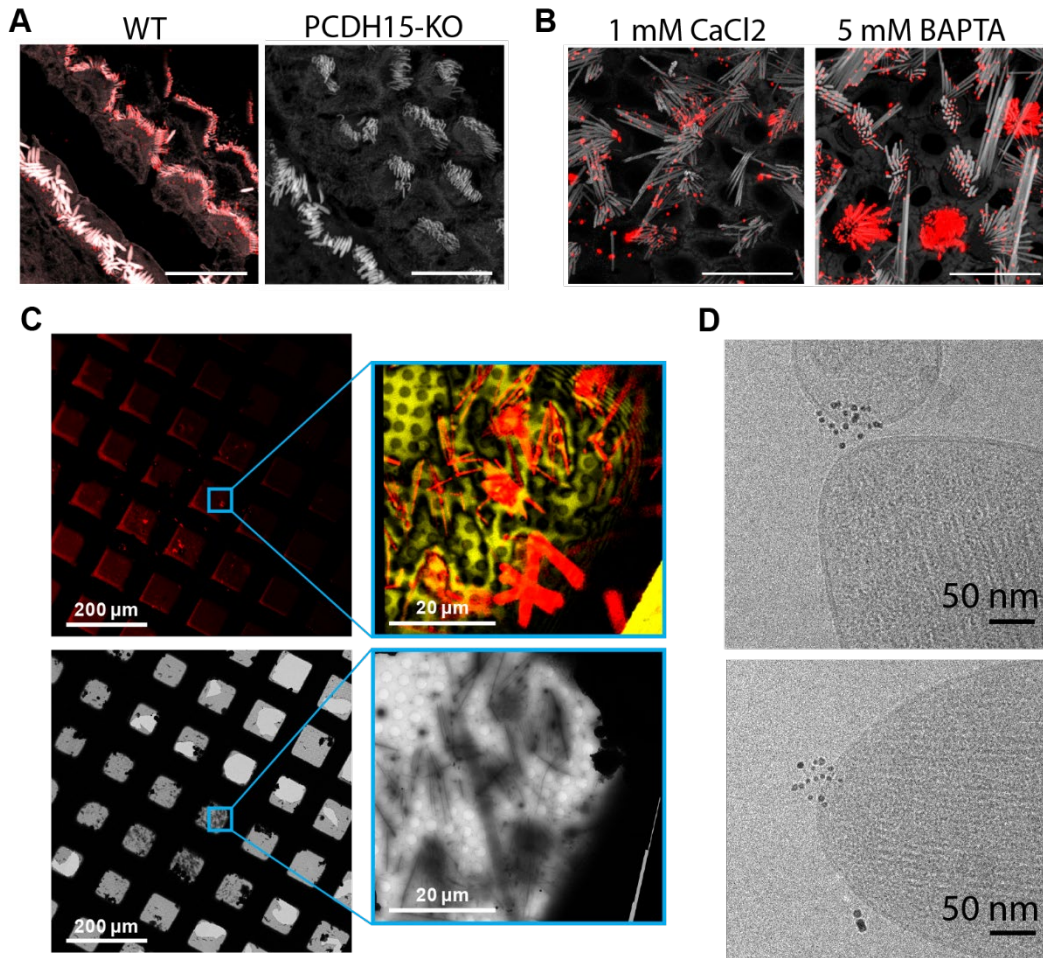
Figure 1. Cryo-EM data-collection of antibody stained stereocilia tips supported by cryo-CLEM

(A) Immunostaining of WT cochlea or PCDH15 KO with polyclonal antibody raised in rabbits against PCDH15 extracellular domain. (B) Immunostaining of WT utricle with polyclonal antibody in media containing 1mM CaCl2 or with the addition of 5mM BAPTA (C) CLEM-based screening to identify squares with thin-ice supported stereocilia. The top row shows low- and medium magnification views acquired using a cryo-light microscope. In both views SirAction fluorescence is shown in red. In the medium-magnification view laser-reflection is shown in gold. The bottom rows show the same areas as acquired in a cryo-TEM. (D) High-

565   magnification cryo-TEM micrographs of stereocilia tips stained with the anti-PCDH15 rabbit

566   polyclonal antibody, detected with a 5nm gold coupled secondary antibody.
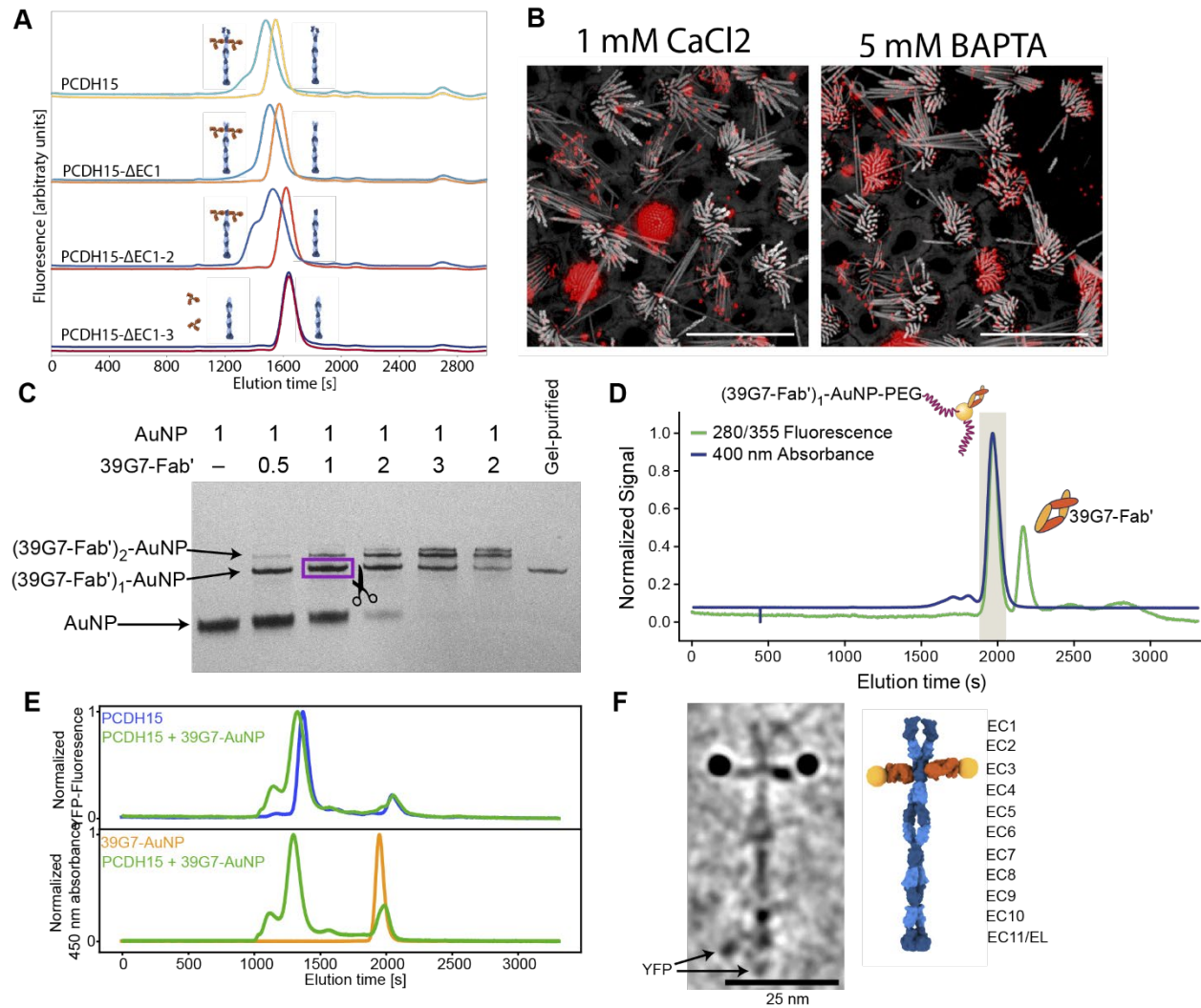
Figure 2. Stoichiometric gold staining of PCDH15 using a monoclonal Fab AuNP conjugate

(A) FSEC analysis of binding of 39G7 to the PCDH15 extracellular domain. 39G7 addition leads to earlier elution of PCDH15 in full-length constructs and after deletion of EC1 and EC2. Deletion of EC3 abolished 39G7 binding. (B) Immunostaining of WT utricle with 39G7 in media containing 1mM CaCl2 or with the addition of 5mM BAPTA. (C) PAGE analysis and purification of conjugation between 39G7 Fab' and a 2nm AuNP (D) SEC purification of PEG-coated 39G7-Fab'-AuNP conjugates. (E) FSEC analysis of 39G7-Fab'-AuNP-PEG conjugate to PCDH15 extracellular domain. (F) Cryo-TEM image of PCDH15 extracellular domain bound to

576   39G7-Fab'-AuNP-PEG conjugate together with model of the complex. In the model PCDH15 is

577   shown in blue, 39G7 Fab in orange, and AuNPs as golden spheres.

578

579
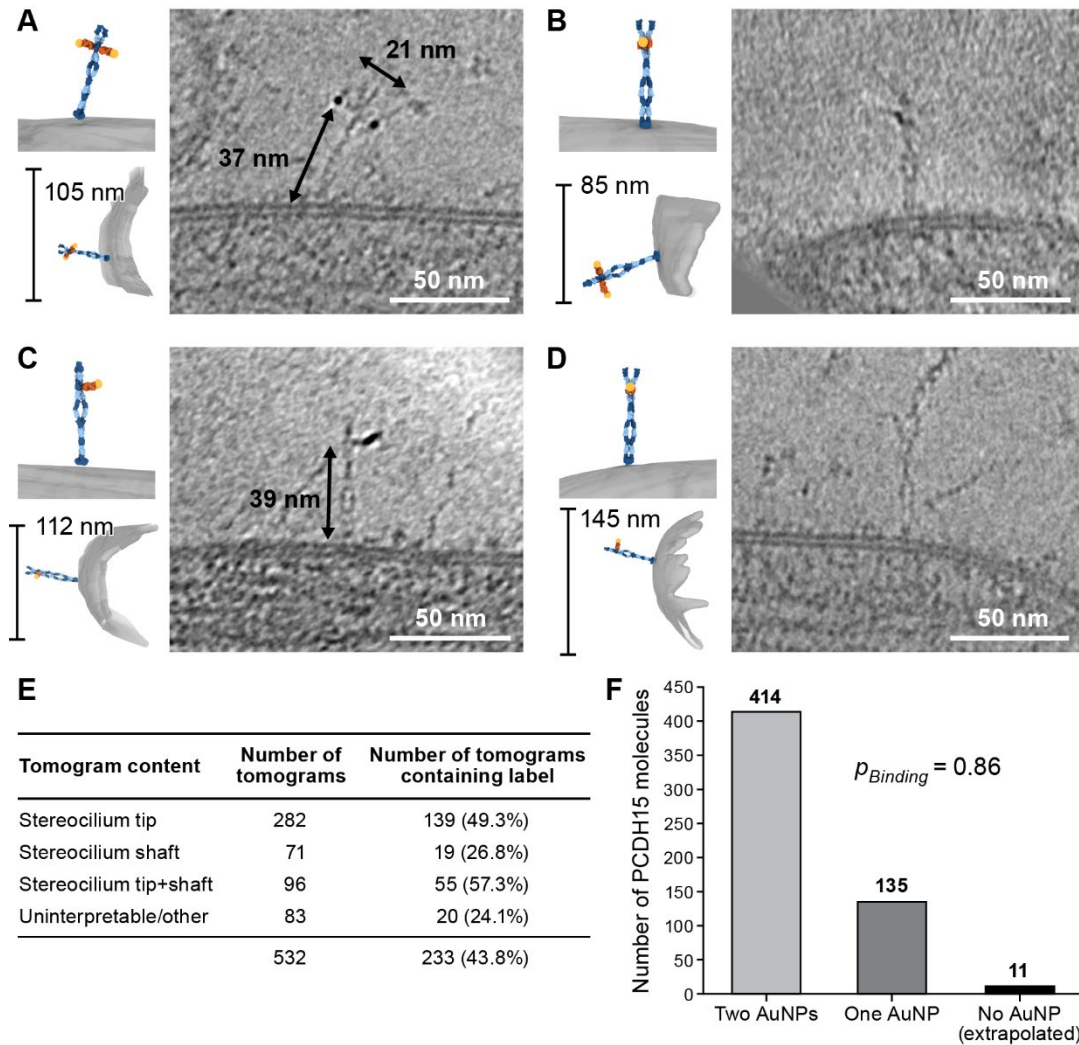
Figure 3. 39G7-AuNP conjugate labels PCDH15 dimer in stereocilia

(A-B) Representative examples of PCDH15 dimers with two bound AuNPs imaged *in situ*. (C-D) Representative examples of PCDH15 dimers with one bound AuNPs imaged *in situ*. Dimeric features in the PCDH15 dens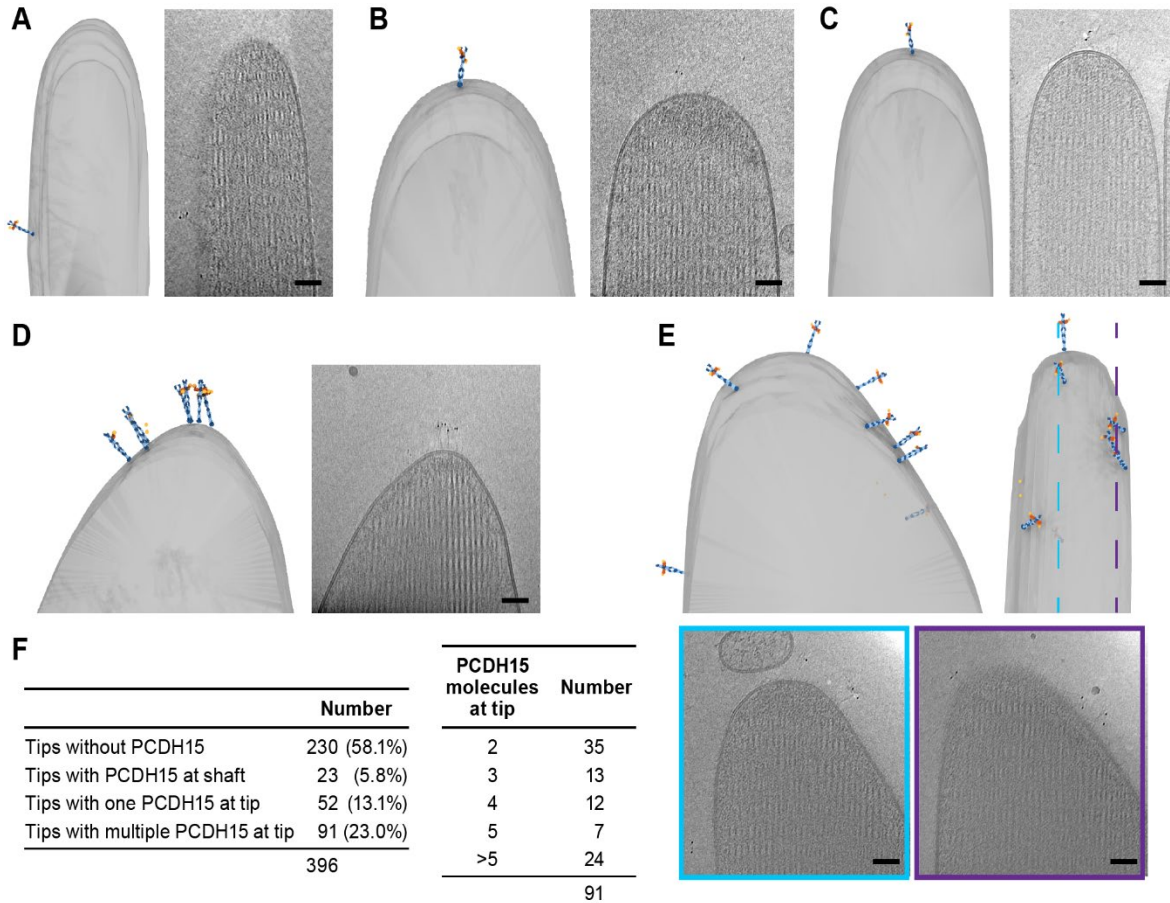ity suggests that these molecules are PCDH15 dimers with one epitope not bound to 39G7. (E) Table detailing numbers and content of collected tomograms. (F) Bar chart quantifying the ratio of PCDH15 molecules labeled by one or two AuNPs. Assuming that AuNPs bind independently to the two epitopes in the PCDH15 dimer results suggests that 86% of all epitopes were labeled and only 2% of PCDH15 molecules were unlabeled.

589

F			PCDH15 molecules at tip	Number
		Number	2	35
Tips without PCDH15		230 (58.1%)	3	13
Tips with PCDH15 at shaft		23 (5.8%)	4	12
Tips with one PCDH15 at tip		52 (13.1%)	5	7
Tips with multiple PCDH15 at tip		91 (23.0%)	>5	24
		396		91

Figure 4. Stereocilia tips frequently harbor more than one copy of PCDH15

(A) Representative example of stereocilia tip with PCDH15 molecule only found in adjacent shaft. (B-C) Representative examples of stereocilia tips with one copy of PCDH15 at tip. (D-E) Representative examples of stereocilia tips with multiple copies of PCDH15 at tip. (F) Table detailing number of imaged stereocilia tips and distribution of PCDH15 molecules found at the tip.
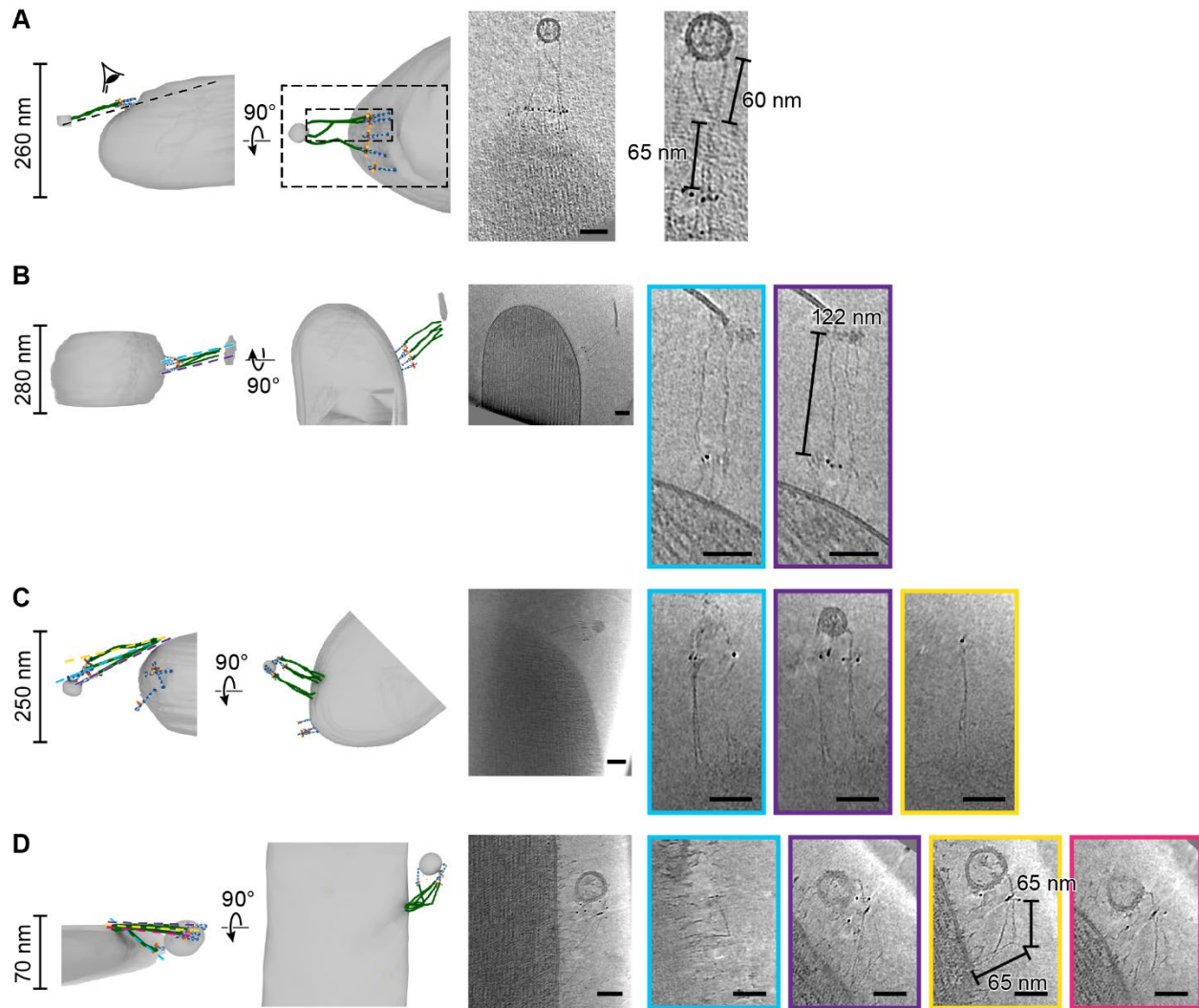
Figure 5. PCDH15/CDH23 tetramers are found in clusters

On the left side of each panel the tomogram annotation is shown from the side and from top. On

the sideview ice thickness is indicated. To the right of the annotation is a projection of the cluster

density in context of the stereocilium. Further to the right are detailed slices of the electron

density. The angle and position of each slice is indicated in the sideview of the tomogram

annotation. Scale bars correspond to 50nm. (A-B) Representative tomograms showing

PCDH15/CDH23 heterotetramers with PCDH15 at tip of stereocilium and CDH23 in lipid

fragment. (C-D) Representative tomograms showing PCDH15/CDH23 heterotetramers with

CDH23 in side of stereocilium and PCDH15 in lipid fragment.
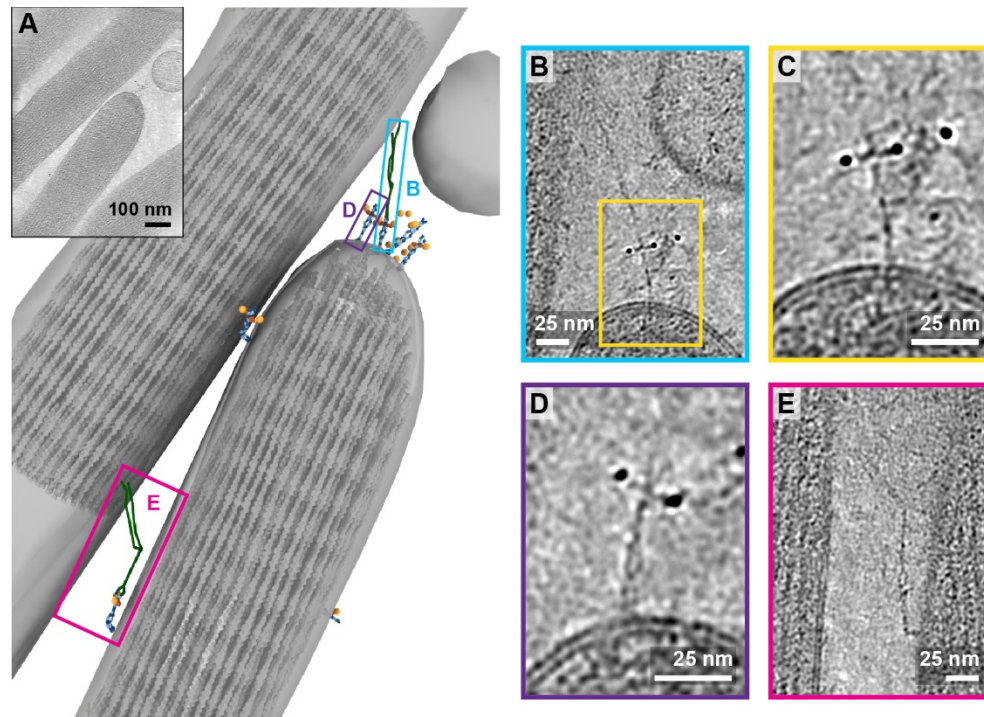
Figure 6. Tomogram containing intact tip-link

(A) Annotation of tomogram showing a putative intact tip-link. The inset at the top left shows a

projection of the tomogram. (B) Closeup view of putative tip-link density in the tomogram. (C)

Closeup of PCDH15 density in tip-link. (D) Close-up of PCDH15 molecule at tip not bound to

CDH23. (E) Close-up of PCDH15/CDH23 heterotetramer in the stereocilia shaft region.

PCDH15 has a 90° bend between EC9 and EC10.
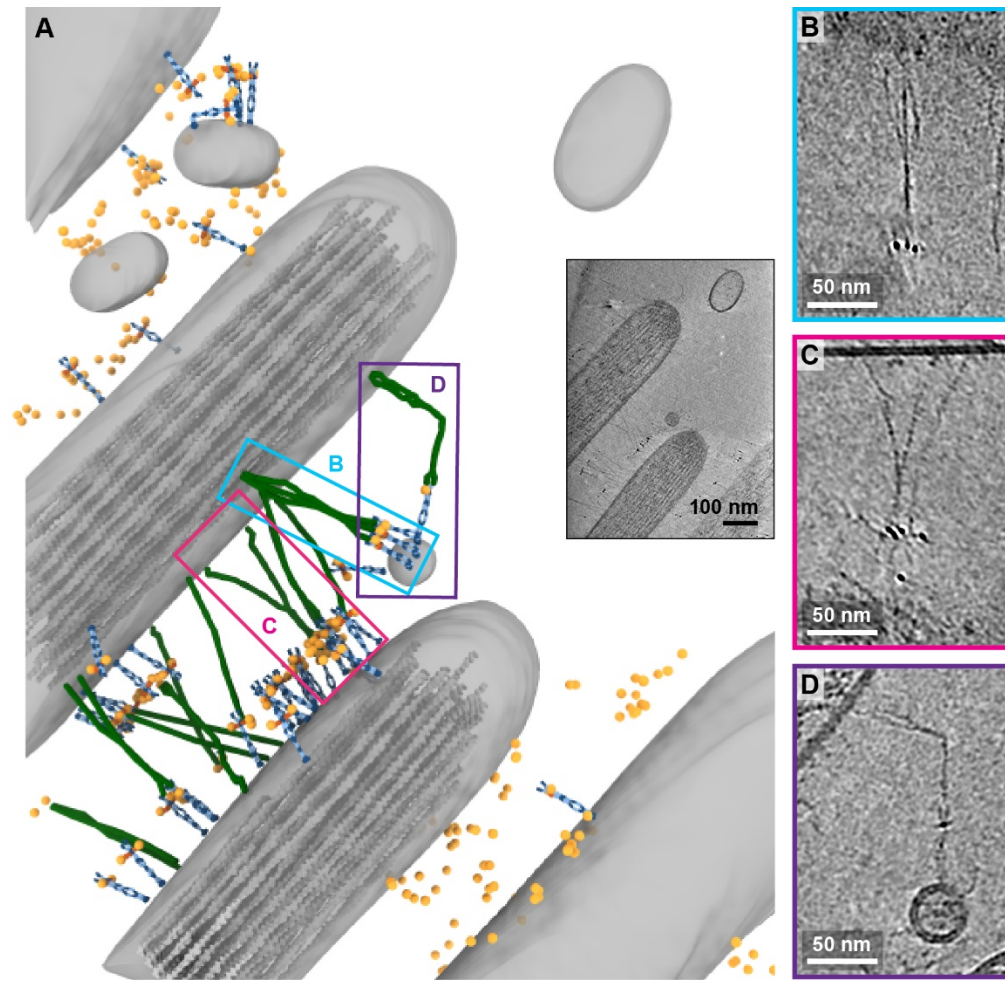
Figure 7. Tomogram depicting lateral links containing PCDH15 in small stereocilia

(A) Annotation of tomogram showing developing stereocilia including PCDH15/CDH23 'lateral links'. The inset at the bottom right shows a projection of the tomogram. (B-C) Closeup of CDH23 molecules clustering together into single strand. (D) Closeup of CDH23 molecule with distinct bend half-way between N- and C-terminal end.

Supplementary Materials

Movie S1. Tomogram of recombinant PCDH15 extracellular domain in complex with 39G7-AuNP conjugate.

Movie S2. Tomogram of stereocilium displaying a PCDH15 dimer with two bound 39G7-AuNP conjugates, also depicted in Figure 3A.

Movie S3. Tomogram of stereocilium displaying a PCDH15 dimer with two bound 39G7-AuNP conjugates, also depicted in Figure 3B.

Movie S4. Tomogram of stereocilium displaying a PCDH15 dimer with one bound 39G7-AuNP conjugates also depicted in Figure 3C.

Movie S5. Tomogram of stereocilium displaying a PCDH15 dimer with one bound 39G7-AuNP conjugates, also depicted in Figure 3D.

Movie S6. Tomogram of stereocilium tip with a single PCDH15 dimer in the shaft region of the tip, also depicted in Figure 4A.

Movie S7. Tomogram of stereocilium tip with a single PCDH15 dimer at the apex of the tip, also depicted in Figure 4B.

Movie S8. Tomogram of stereocilium tip with a single PCDH15 dimer at the apex of the tip, also depicted in Figure 4C.

Movie S9. Tomogram of stereocilium tip with a cluster of multiple PCDH15 dimers at the apex of the tip, also depicted in Figure 4D.

Movie S10. Tomogram of stereocilium tip with multiple PCDH15 dimers scattered around the tip, also depicted in Figure 4E.

Movie S11. Tomogram of stereocilium tip containing multiple PCDH15 dimers connected to putative CDH23 filaments in a lipid vesicle, also depicted in Figure 5A.

645   **Movie S12.** Tomogram of stereocilium tip containing multiple PCDH15 dimers connected to

646   putative CDH23 filaments in a lipid membrane fragment, also depicted in Figure 5B.

647   **Movie S13.** Tomogram of a stereocilium tip containing multiple putative CDH23 filaments

648   connected to PCDH15 dimers in a lipid vesicle, also depicted in Figure 5C.

649   **Movie S14.** Tomogram of a stereocilium shaft containing multiple putative CDH23 filaments

650   connected to PCDH15 dimers in a lipid vesicle, also depicted in Figure 5D.

651   **Movie S15.** Tomogram of a stereocilium tip and a stereocilium shaft containing a PCDH15

652   dimer in the stereocilium tip that is connected to a putative CDH23 filament in the neighboring

653   stereocilium shaft. The tip also contains PCDH15 dimers not bound to CDH23. An additional

654   putative PCDH15/CDH23 complex is connecting the two stereocilia in the shaft region. Also

655   depicted in Figure 6.

656   **Movie S16**. Tomogram of stereocilia connected by tens of PCDH15/CDH23 complexes.

657   Noteworthy complexes, that include apparent interaction between CDH23 dimers, as well as

658   bends in the CDH23 dimer are highlighted. Also depicted in Figure 7.